# Modeling of the Evaporation and Condensation Phase-Change Problems with FLUENT

Dongliang Sun [a] [b], Jinliang Xu [a] [b] & Qicheng Chen [b]

[a] State Key Laboratory of Alternate Electrical Power System with Renewable Energy Sources, North China Electric Power University, Beijing, People's Republic of China

[b] Beijing Key Laboratory of Multiphase Flow and Heat Transfer, North China Electric Power University, Beijing, People's Republic of China
Published online: 25 Aug 2014.

PLEASE SCROLL DOWN FOR ARTICLE

Taylor & Francis
Taylor & Francis Group

# MODELING OF THE EVAPORATION AND CONDENSATION PHASE-CHANGE PROBLEMS WITH FLUENT

## Dongliang Sun[1,2], Jinliang Xu[1,2], and Qicheng Chen[2]

[1]*State Key Laboratory of Alternate Electrical Power System with Renewable Energy Sources, North China Electric Power University, Beijing, People's Republic of China*
[2]*Beijing Key Laboratory of Multiphase Flow and Heat Transfer, North China Electric Power University, Beijing, People's Republic of China*

*Based on the volume-of-fluid (VOF) method in the FLUENT code, many phase-change models have been proposed and applied to simulate evaporation and condensation problems. To further improve the accuracy, in this article a new phase-change model is built using user-defined functions (UDFs). The accuracy of this new phase-change model is verified by two evaporation problems (a one-dimensional Stefan problem and a two-dimensional film boiling problem) and one condensation problem (single steam bubble condensation in subcooled water). The simulation results of this new model show good agreement with the classical analytical or numerical results, proving its accuracy and feasibility.*

## 1. INTRODUCTION

Evaporation and condensation play a very significant role in most important industrial processes, just to mention perspective applications in removal of large heat fluxes in electronics and power engineering. Evaporation is the process of turning a liquid, at its saturation temperature, into vapor by applying heat. The process reverse to evaporation is condensation, where vapor turns into liquid due to the removal of heat. There have been many experimental analyses to explain the evaporation and condensation phenomena. However, it is very difficult to thoroughly reveal these phenomena by experimental measures. Therefore, it is necessary to carry out numerical simulations as a complement to experiments. Such numerical simulations may contribute to a better physical understanding of complex evaporation and condensation phenomena.

Many methods have been proposed to simulate the vapor–liquid phase-change problems, such as the volume-of-fluid (VOF) method [1–3] and the level set (LS)

Color versions of one or more of the figures in the article can be found online at www.tandfonline.com/unhb.

## NOMENCLATURE

| | | | | |
|---|---|---|---|---|
| $A$ | area, $m^2$ | | $\alpha$ | volume fraction |
| $C$ | grid cell | | $\delta$ | interface position, m |
| $C_I$ | grid cell where the interface exists | | $\kappa$ | interface curvature, $m^{-1}$ |
| $C_{Is}$ | grid cell occupied by the saturated phase next to $C_I$ | | $\lambda$ | thermal conductivity, W/m K |
| | | | $\lambda_0$ | unstable Taylor wavelength, m |
| $C_p$ | specific heat, J/kg K | | $\lambda'$ | characteristic length, m |
| $F_V$ | interface-induced volume force, $N/m^3$ | | $\mu$ | dynamic viscosity, Pa s |
| $g$ | gravity acceleration, $m/s^2$ | | $\rho$ | density, $kg/m^3$ |
| $h$ | apparent energy with the zero defined at 298.15 K, J/kg | | $\sigma$ | surface tension coefficient, N/m |
| $h_{fg}$ | latent heat, J/kg | | **Subscripts** | |
| $\dot{m}$ | interfacial mass transfer flux, $kg/m^3$ s | | $C$ | grid cell |
| $\vec{n}$ | unit normal vector | | $C_I$ | grid cell where the interface exists |
| Nu | Nusselt number | | $C_{Is}$ | grid cell occupied by the saturated phase next to $C_I$ |
| $p$ | pressure, Pa | | | |
| $\|\vec{q}_I\|$ | interfacial heat flux jump, $W/m^2$ | | $f$ | cell face |
| $Q$ | heat, w | | $I$ | interface |
| $r$ | mass transfer intensity factor, $s^{-1}$; coordinate, m | | in | inside of grid cell |
| | | | $l$ | liquid phase |
| $S_h$ | heat source term due to phase change, $W/m^3$ | | out | outside of grid cell |
| | | | $s$ | saturated phase |
| $t$ | time, s | | sat | saturated temperature |
| $T$ | temperature, K | | uns | unsaturated phase |
| $v$ | velocity, m/s | | $v$ | vapor phase |
| $V$ | volume, $m^3$ | | $V$ | volume |
| $x, y$ | coordinates, m | | $w$ | wall |

method [4–6]. The VOF method has an inherent mass conservation property, more easily capturing interface with heat transfer of phase change [7]. The feature of mass conservation is particularly important when solving phase-change problems [8]. Therefore, it is a good choice to use the VOF method. At present, the VOF method has been employed in the FLUENT code to solve two-phase flows. However, the default VOF method cannot simulate heat and mass transfer through the phase interface. To overcome this short coming, the phase-change model needs to be added to the source terms in the governing equations using user-defined functions (UDFs).

There are many different kinds of phase-change models in references. The use of empirical expressions to quantify the interfacial heat and mass transfer appears to be a common way to model the phase-change phenomena [9, 10]. The approach is indeed valuable for certain simple geometries. However, its application is limited for any other geometry [11].

The phase-change model proposed by Lee [12] has been most widely used. The mass transfers are given by the following equations:

$$\dot{m}_v = -\dot{m}_l = r\alpha_l\rho_l\frac{T - T_{\text{sat}}}{T_{\text{sat}}} \quad T > T_{\text{sat}} \text{ (evaporation process)} \tag{1}$$

$$\dot{m}_l = -\dot{m}_v = r\alpha_v\rho_v\frac{T_{\text{sat}} - T}{T_{\text{sat}}} \quad T < T_{\text{sat}} \text{ (condensation process)} \tag{2}$$

where $r$ denotes the mass transfer intensity factor with unit $\text{s}^{-1}$. The value of $r$ is recommended to be such as to maintain the interfacial temperature reasonably close to the saturation temperature, and to avoid divergence issues. As an empirical coefficient, $r$ is given different values for different problems. In the numerical studies of Wu et al. [13], De Schepper et al. [14], and Alizadehdakhel et al. [15], $r$ was set as $0.1\,\text{s}^{-1}$ in order to numerically maintain the interface temperature close to the saturation temperature. However, $r$ was specified at a different value, $100\,\text{s}^{-1}$, in [16] and [17].

To avoid the limitation of empirical expressions or empirical coefficients, it is essential to develop a purely theoretical and validated formulation that explicitly solves phase-change problems. Fourier's law, as a theoretical formulation, can be applied to estimate the interfacial heat flux jump and determine the corresponding mass transfer flux based on the latent heat. The interfacial heat flux jump and mass transfer flux can be calculated by the following expressions:

$$||\vec{q}_I|| = \left[\left(-\lambda_l\frac{\partial T}{\partial n}\Big|_l\right) - \left(-\lambda_v\frac{\partial T}{\partial n}\Big|_v\right)\right]\vec{n} \tag{3}$$

$$\dot{m}_l = -\dot{m}_v = \frac{(||\vec{q}_I|| \cdot \vec{n})A_{I,C}}{h_{fg}V_C} \tag{4}$$

where $\vec{n}$ is the interfacial unit normal vector and points toward the liquid phase. $A_{I,C}$ and $V_C$ denote, respectively, the interface area in a grid cell and the corresponding grid cell volume.

According to Eqs. (3) and (4), many authors have developed their own program codes to simulate phase-change problems, such as Welch and Wilson [7] and Guo et al. [18]. The key point of these models is how to accurately calculate the heat fluxes on both sides of the interface. These models can simulate the evaporation and condensation problems accurately. However, the implementation process is very complicated, limiting the extension of these models to the FLUENT code.

In [11], [19], and [20], the following phase-change model was derived according to Eqs. (3) and (4):

$$\dot{m}_v = -\dot{m}_l = \frac{(\alpha_v\lambda_v + \alpha_l\lambda_l)(\nabla\alpha_l \cdot \nabla T)}{h_{fg}} \tag{5}$$

which is easy to implement in the FLUENT code. However, this model has some shortcomings. For example, the bubble growth rate is not relevant to the vapor thermal conductivity $\lambda_v$ in the growing process of a saturated bubble in superheated liquid. However, Eq. (5) contains the information of $\lambda_v$, not matching the actual physical phenomena.

To overcome the shortcomings mentioned above, a phase-change model [21] was proposed by the present authors in 2012 as follows:

$$\dot{m}_v = -\dot{m}_l = \frac{2\lambda_l(\nabla\alpha_l \cdot \nabla T)}{h_{fg}} \tag{6}$$

As we know, the mass transfer appears at the phase interface. However, the interfacial mass transfer fluxes calculated by Eqs. (5) and (6) are distributed in a finite-thickness region near the interface, reducing the calculation accuracy.

In this article, to further improve the accuracy, a new phase-change model is built based on the volume-of-fluid (VOF) method in the FLUENT code. Finally, the accuracy of this new phase-change model is verified by two evaporation problems (a one-dimensional Stefan problem and a two-dimensional film boiling problem) and one condensation problem (single steam bubble condensation in subcooled water).

## 2. GOVERNING EQUATIONS AND NEW PHASE-CHANGE MODEL

The phase-change processes considered in this article are incompressible, laminar, and unsteady two-phase flow and heat transfer problems. In the following, we will introduce the governing equations and the new phase-change model in detail.

### 2.1. Governing Equations

In 1981, Hirt and Nichols [1] developed the volume-of-fluid (VOF) method, in which a volume fraction $\alpha$ is defined. The value of the volume fraction lies between 0 and 1, and the sum of the volume fractions of all phases equals 1 in each grid cell:

$$\alpha_l + \alpha_v = 1 \tag{7}$$

The governing equations of the volume fractions can be written as follows:

$$\frac{\partial \alpha_l}{\partial t} + \nabla \cdot (\vec{v}\alpha_l) = \frac{\dot{m}_l}{\rho_l} \tag{8}$$

$$\frac{\partial \alpha_v}{\partial t} + \nabla \cdot (\vec{v}\alpha_v) = \frac{\dot{m}_v}{\rho_v} \tag{9}$$

where $\dot{m}_l = -\dot{m}_v$.

The momentum equation can be expressed as follows:

$$\frac{\partial}{\partial t}(\rho\vec{v}) + \nabla \cdot (\rho\vec{v}\vec{v}) = -\nabla p + \nabla \cdot [\mu(\nabla\vec{v} + \nabla\vec{v}^T)] + \rho\vec{g} + F_V \tag{10}$$

where

$$\rho = \rho_l\alpha_l + \rho_v\alpha_v \tag{11}$$

$$\mu = \mu_l\alpha_l + \mu_v\alpha_v \tag{12}$$

As we all know, surface tension is a surface force. In order to add the surface tension to the source term in the momentum equation, Brackbill converted the surface force into a volume force, $F_V$, by the continuum surface force (CSF) model [22]. $F_V$ can be expressed as follows:

$$F_V = \sigma \frac{\alpha_l\rho_l\kappa_l\nabla\alpha_l + \alpha_v\rho_v\kappa_v\nabla\alpha_v}{0.5(\rho_l + \rho_v)} \tag{13}$$

where the interface curvature is obtained from

$$\kappa_l = -\kappa_v = -\nabla \cdot \left( \frac{\nabla \alpha_l}{|\nabla \alpha_l|} \right) \tag{14}$$

The energy equation can be expressed as follows:

$$\frac{\partial}{\partial t}(\rho h) + \nabla \cdot (\rho \vec{v} h) = \nabla \cdot (\lambda \nabla T) + S_h \tag{15}$$

where

$$h = \frac{\alpha_l \rho_l h_l + \alpha_v \rho_v h_v}{\alpha_l \rho_l + \alpha_v \rho_v} \tag{16}$$

$$h_l = C_{p,l}(T - 298.15) \quad h_v = C_{p,v}(T - 298.15) \tag{17}$$

$$\lambda = \lambda_l \alpha_l + \lambda_v \alpha_v \tag{18}$$

### 2.2. New Phase-Change Model

The new phase-change model is developed using the user-defined functions (UDFs) in the FLUENT code. The UDF is a routine written in the C programming language and is based on the FLUENT macro. Finally, the developed UDFs for solving $\dot{m}_l$, $\dot{m}_v$, and $S_h$ are compiled and linked with the source terms in Eqs. (8), (9), and (15).

This model is suitable for the case in which one phase is unsaturated and the other is saturated. In the following, we will introduce its implementation process.

**1. Assume that the thermal conductivity of the saturated phase is equal to that of the unsaturated phase, i.e., $\lambda_s = \lambda_{uns}$.**

For the case in which one phase is unsaturated and the other is saturated, the interfacial heat flux jump can be expressed as

$$||\vec{q}_I|| = \left( -\lambda_{uns} \frac{\partial T}{\partial n} \Big|_{uns} \right) \vec{n} \tag{19}$$

which is determined by $\lambda_{uns}$ and is independent of $\lambda_s$. Therefore, $\lambda_s$ is assumed to equal to $\lambda_{uns}$.

**2. Calculate the interfacial mass transfer fluxes ($\dot{m}_l$ and $\dot{m}_v$).**

Two types of grid cells are labeled in Figure 1. The first is the grid cell where the interface exists, labeled as $C_I$. The second is the grid cell occupied by the saturated phase next to $C_I$, labeled as $C_{Is}$.

For the condensation process, the interfacial mass transfer fluxes at $C_I$ are determined by the heat exported from $C_I$ and $C_{Is}$. The heat exported from $C_I$ can be expressed as

$$Q_{C_I,\text{out}} = \sum_{f \in C_I} \max\{(-\lambda_{uns} A_f \nabla T_f) \cdot \vec{n}_{f,\text{out}}, 0\} \tag{20}$$
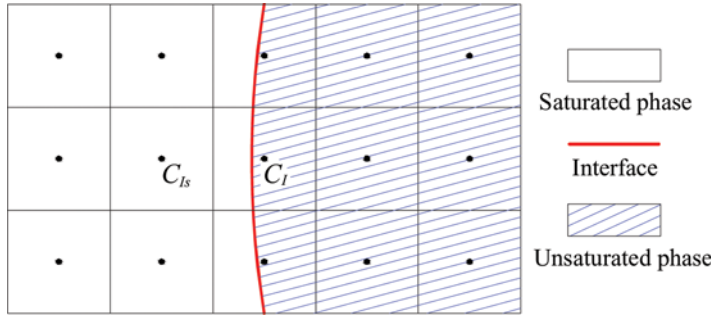
**Figure 1.** Schematic diagram of two types of grid cells, $C_I$ and $C_{Is}$.

where $f$ denotes the face of $C_I$, $A_f$ is the face area, $\nabla T_f$ is the temperature gradient at the cell face, $\vec{n}_{f,\text{out}}$ is the unit normal vector at the cell face and points outside of $C_I$.

The heat exported from $C_{Is}$ can be expressed as

$$Q_{C_{Is},\text{out}} = \sum_{f \in C_{Is}} \max\left\{(-\lambda_{\text{uns}} A_f \nabla T_f) \cdot \vec{n}_{f,\text{out}}, 0\right\} \tag{21}$$

Then the interfacial mass transfer fluxes at $C_I$ can be calculated by $Q_{C_I,\text{out}}$ and $Q_{C_{Is},\text{out}}$ for the condensation process.

$$\dot{m}_l = -\dot{m}_v = \frac{Q_{C_I,\text{out}}}{h_{fg} V_{C_I}} + \frac{Q_{C_{Is},\text{out}}}{h_{fg} V_{C_{Is}}} \quad \text{at } C_I \quad \text{(condensation process)} \tag{22}$$

For the evaporation process, the interfacial mass transfer fluxes at $C_I$ are determined by the heat imported in $C_I$ and $C_{Is}$. The heat imported in $C_I$ can be expressed as

$$Q_{C_I,\text{in}} = \sum_{f \in C_I} \max\left\{(-\lambda_{\text{uns}} A_f \nabla T_f) \cdot \vec{n}_{f,\text{in}}, 0\right\} \tag{23}$$

The heat imported in $C_{Is}$ can be expressed as

$$Q_{C_{Is},\text{in}} = \sum_{f \in C_{Is}} \max\left\{(-\lambda_{\text{uns}} A_f \nabla T_f) \cdot \vec{n}_{f,\text{in}}, 0\right\} \tag{24}$$

Then the interfacial mass transfer fluxes at $C_I$ can be calculated by $Q_{C_I,\text{in}}$ and $Q_{C_{Is},\text{in}}$ for the evaporation process.

$$\dot{m}_v = -\dot{m}_l = \frac{Q_{C_I,\text{in}}}{h_{fg} V_{C_I}} + \frac{Q_{C_{Is},\text{in}}}{h_{fg} V_{C_{Is}}} \quad \text{at } C_I \text{ (evaporation process)} \tag{25}$$

### 3. Calculate the heat source term ($S_h$).

For the condensation process, the heat source term can be written as

$$S_h = \begin{cases} Q_{C_I,\text{out}}/V_{C_I} & \text{at } C_I \\ 10^{30}T_{\text{sat}} - 10^{30}T_{C_{Is}} & \text{at } C_{Is} \end{cases} \quad \text{(condensation process)} \qquad (26)$$

where the large coefficient method [23] is adopted to set the temperature at $C_{Is}$ as the saturated temperature.

For the evaporation process, the heat source term can be expressed as

$$S_h = \begin{cases} Q_{C_I,\text{in}}/V_{C_I} & \text{at } C_I \\ 10^{30}T_{\text{sat}} - 10^{30}T_{C_{Is}} & \text{at } C_{Is} \end{cases} \quad \text{(evaporation process)} \qquad (27)$$

## 3. VERIFICATION OF THE PHASE-CHANGE MODEL

The accuracy of this new phase-change model is verified by two evaporation problems (a one-dimensional Stefan problem and a two-dimensional film boiling problem) and one condensation problem (single steam bubble condensation in subcooled water). In the process of solving the problems mentioned above, the governing equations of the volume fractions [Eqs. (8) and (9)] are solved by the geometric reconstruction scheme (PLIC) [2]. The second-order upwind scheme is adopted for the convection terms in the momentum equation [Eq. (10)] and the energy equation [Eq. (15)]. The SIMPLE algorithm is used to couple the velocity and pressure. The first-order implicit scheme treats the time marching. The time step $\Delta t$ is controlled by a specified maximum value for the Courant number, which is defined as

$$\text{Co} = \frac{\Delta t}{\Delta x/|\vec{v}|} \qquad (28)$$

where $\Delta x$ is the grid size and $|\vec{v}|$ is the fluid velocity within the grid. We set a maximum Courant number of 0.25 and use a variable time step based on the Courant number.

### 3.1. One-Dimensional Stefan Problem

Figure 2 shows a schematic diagram of the one-dimensional Stefan problem, which has served over and over again as a benchmark problem for testing new models [7, 18, 20, 24]. In this problem, the wall temperature is higher than the saturated temperature. The vapor near the wall experiences an increase in temperature and becomes superheated, which drives mass transfer at the interface.

The exact interface positions with time (analytical solutions) may be calculated by the equation [25]

$$\delta(t) = 2\varepsilon\sqrt{\frac{\lambda_v t}{\rho_v C_{p,v}}} \qquad (29)$$
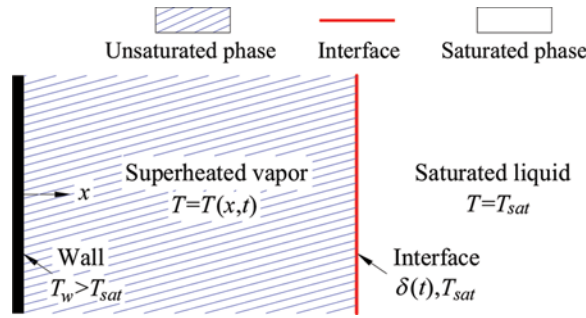
**Figure 2.** Schematic diagram of one-dimensional Stefan problem.

where ε is a solution to the transcendental equation

$$\varepsilon \exp(\varepsilon^2)\, \mathrm{erf}(\varepsilon) = \frac{C_{p,v}(T_w - T_{\mathrm{sat}})}{h_{fg}\sqrt{\pi}} \qquad (30)$$

In this problem, the unsaturated phase is superheated vapor. Three different vapor densities are considered, $\rho_v = 0.001$, $0.01$, and $0.1\,\mathrm{kg/m^3}$. The vapor thermal conductivity $\lambda_v = 0.005\,\mathrm{w/m\,K}$) and specific heat $C_{p,v} = 200\,\mathrm{J/kg\,K}$. The saturated phase is saturated liquid and its density $\rho_l = 1\,\mathrm{kg/m^3}$. Latent heat $h_{fg} = 10^4\,\mathrm{J/kg}$. The difference between the wall and the saturated temperatures $\Delta T = T_w - T_{\mathrm{sat}} = 10\,\mathrm{K}$.

A grid independence test is performed using three different grid systems. The grid numbers considered in this problem are $100(x)$, $200(x)$, and $400(x)$ in the length $0.2\,\mathrm{m}$. As shown in Figure 3, the simulated results are almost the same for the three different grid systems, verifying the gird independence. Thus, a $200(x)$ gird mesh is used for later simulations.

Figure 4 shows the interface positions with time at three different density ratios ($\rho_l/\rho_v = 10$, $100$, $1,000$). As shown in this figure, the simulation results agree very well
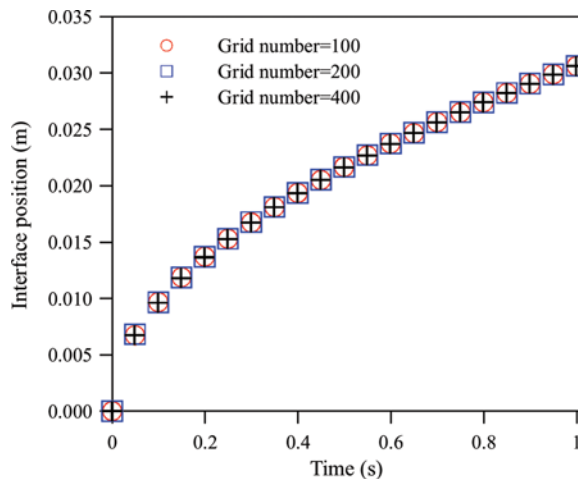


**Figure 3.** Interface positions with time for three different grid systems ($\rho_l/\rho_g = 100$).
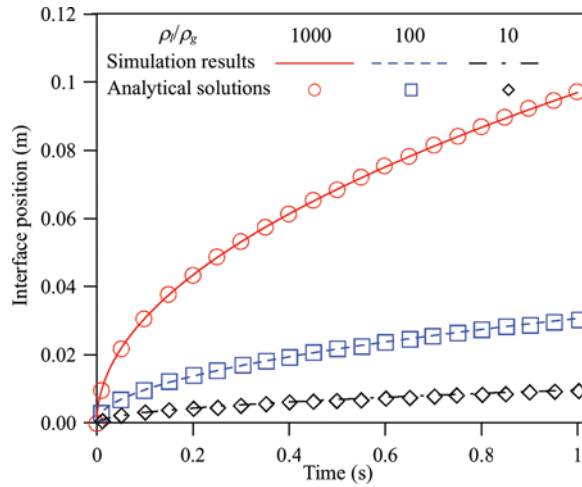
**Figure 4.** Interface positions with time for three different density ratios.

with the exact analytical solutions, verifying the accuracy of this phase-change model. The temperature distributions at $t = 1\,\mathrm{s}$ are shown in Figure 5 for three different density ratios. The liquid can be maintained at the saturation temperature, further verifying the accuracy of the model.
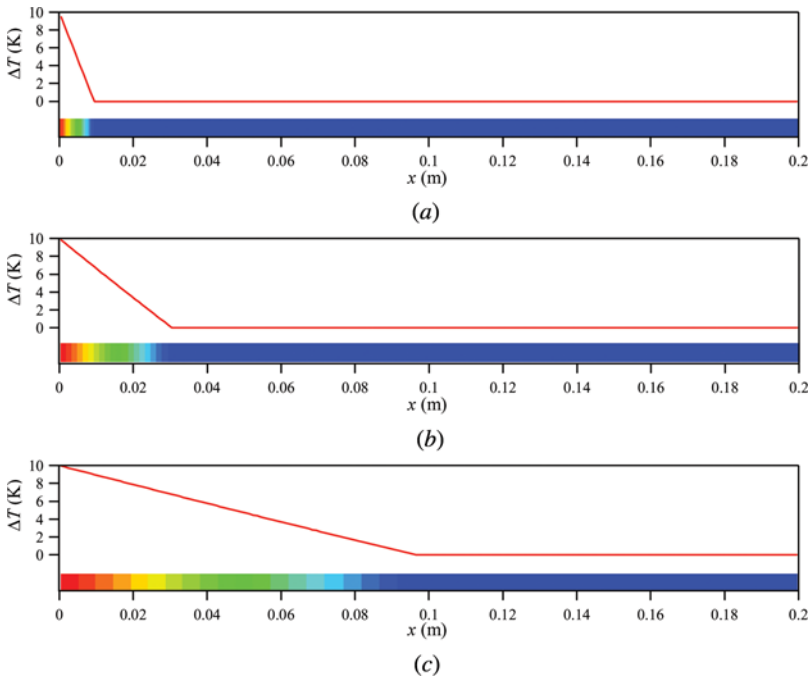


**Figure 5.** Temperature distributions at $t = 1\,\mathrm{s}$ for three different density ratios. (a) $\rho_l/\rho_g = 10$, (b) $\rho_l/\rho_g = 100$ and (c) $\rho_l/\rho_g = 1000$.
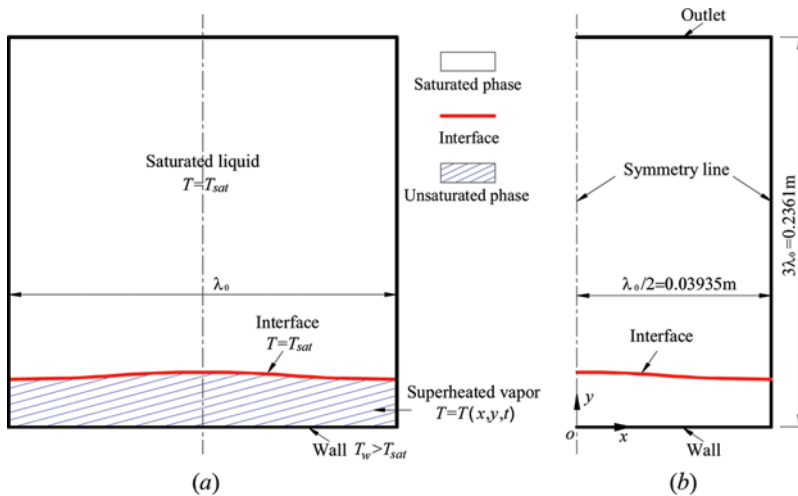
### 3.2. Two-Dimensional Film Boiling Problem

Figure 6a shows a schematic diagram of the two-dimensional boiling problem. The bottom wall is covered by a layer of superheated vapor which is located below the saturated liquid. In this problem, the unsaturated phase is superheated vapor. $\rho_v = 5\,\text{kg/m}^3$, $\mu_v = 0.005\,\text{Pa s}$, $\lambda_v = 1\,\text{w/m K}$ and $C_{p,v} = 200\,\text{J/kg K}$. The saturated phase is saturated liquid. $\rho_l = 200\,\text{kg/m}^3$ and $\mu_l = 0.1\,\text{Pa s}$. Latent heat $h_{fg} = 10^4\,\text{J/kg}$, surface tension coefficient $\sigma = 0.1\,\text{N/m}$, and gravity acceleration $g = 9.81\,\text{m/s}^2$. The unstable Taylor wavelength $\lambda_0$, shown in Figure 6a, is calculated by

$$\lambda_0 = 2\pi\sqrt{\frac{3\sigma}{(\rho_l - \rho_g)g}} \qquad (31)$$

Due to the symmetry of the flow configuration, half of the region is selected as the computational region, as shown in Figure 6b. The width and height of the computational region are, respectively, $\lambda_0/2$ and $3\lambda_0$. The no-slip velocity boundary condition is applied on the bottom wall, i.e., $u = v = 0$. The wall temperature is 5 K higher than the saturated temperature, i.e., $\Delta T = T_w - T_{sat} = 5\,\text{K}$. The left and right vertical symmetry lines are set as symmetry boundary conditions. The top outlet is considered as a pressure outlet boundary condition. We initialize the velocity to be zero, the liquid temperature to be saturated temperature, and the vapor temperature to increase linearly for the interface to the wall. The initial interface position can be calculated by

$$y = \frac{\lambda_0}{128}\left[4.0 + \cos\left(\frac{2\pi x}{\lambda}\right)\right] \qquad (32)$$

In order to obtain gird-independent results, three different grid systems of $50(x) \times 300(y)$, $100(x) \times 600(y)$, and $200(x) \times 1200(y)$ are considered. Figure 7



**Figure 6.** Schematic diagram and computational region of two-dimensional film boiling problem. (a) Schematic diagram and (b) computational region.
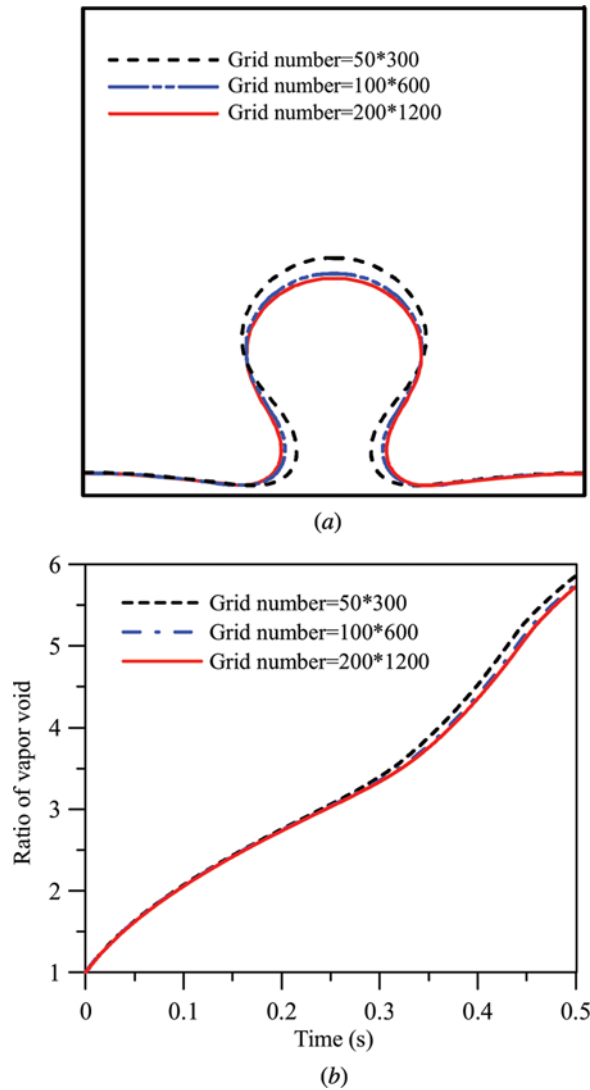
**Figure 7.** Simulation results for three different grid systems. (*a*) Bubble shape at $t = 0.42$ s and (*b*) ratios of vapor void to initial vapor void.

shows the bubble shapes at $t = 0.42$ s and the ratios of vapor void to initial vapor void computed using the three grids. According to these figures, we find that the $100(x) \times 600(y)$ grid system can obtain grid-independent results. Thus, this grid is used in the later simulation.

Film boiling is a quasi-steady phase-change phenomenon, whose behavior has been studied in [7] and [18]. Figure 8 shows the early transients typified by the release of a few larger bubbles before arriving at the quasi-steady bubble patterns (Figure 9). The results computed by the new phase-change model are consistent with those reported by Guo et al. [18].
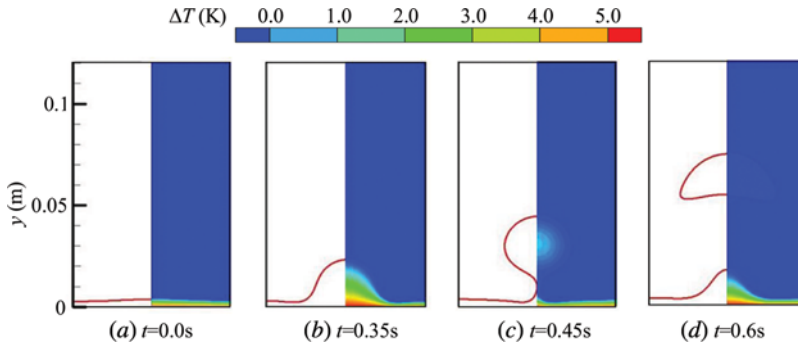
**Figure 8.** Bubble patterns and temperature distributions at early instant (*right*, bubble pattern; *left*, temperature distribution).
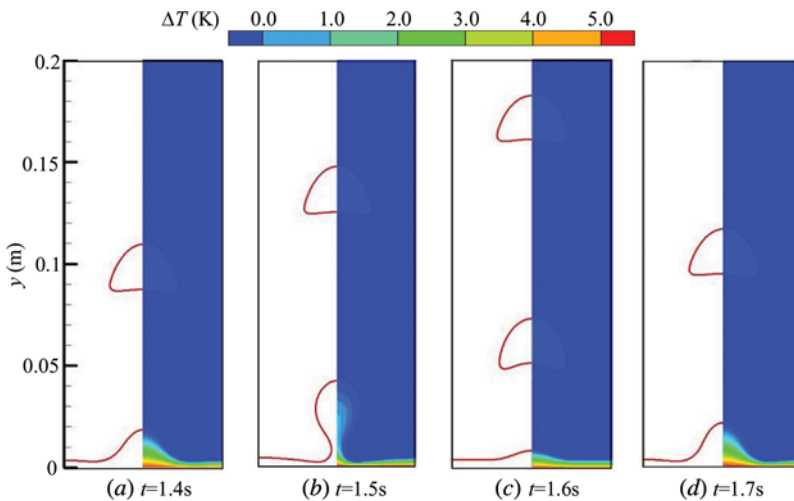
The Nusselt number at the bottom wall is defined as

$$\mathrm{Nu} = \int\limits_{0}^{\lambda_0/2} \left( \frac{\lambda'}{T_w - T_{\mathrm{sat}}} \frac{\partial T}{\partial y}\bigg|_{y=0} \right) dx \bigg/ \frac{\lambda_0}{2} \tag{33}$$

where $\lambda'$ is the characteristic length,

$$\lambda' = \sqrt{\frac{\sigma}{(\rho_l - \rho_v)g}} \tag{34}$$

The Nusselt number calculated by our phase-change model is shown in Figure 10, presenting a periodic change with time. The corresponding time-averaged Nusselt number is 1.83, which is only a 4 % deviation from the result of Klimenko [26].



**Figure 9.** Quasi-steady bubble patterns and temperature distributions (*right*, bubble pattern; *left*, temperature distribution).
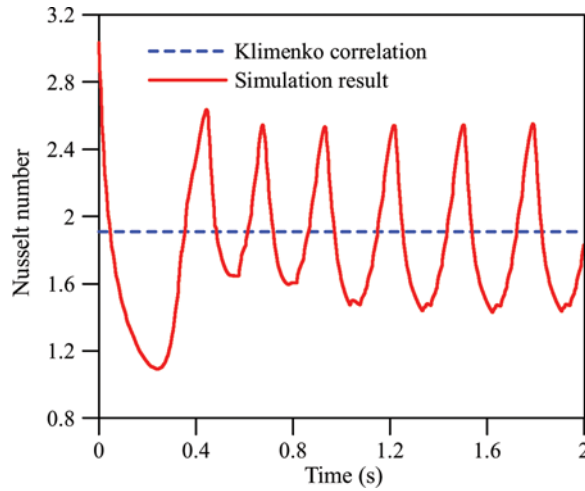
**Figure 10.** Nusselt number for two-dimensional film boiling problem.

## 3.3. Single Bubble Condensation in Subcooled Water

A spherical saturated bubble is located in a cylindrical pool filled with sub-cooled water, as shown in Figure 11a. All physical properties of water and steam are constant under standard atmospheric pressure. Due to the configuration and flow symmetries, the two-dimensional axial-symmetric coordinate ($r$–$x$) system is selected to perform the numerical simulations. Figure 11b shows the corresponding computation region. The radius and height of the computational region are, respectively,
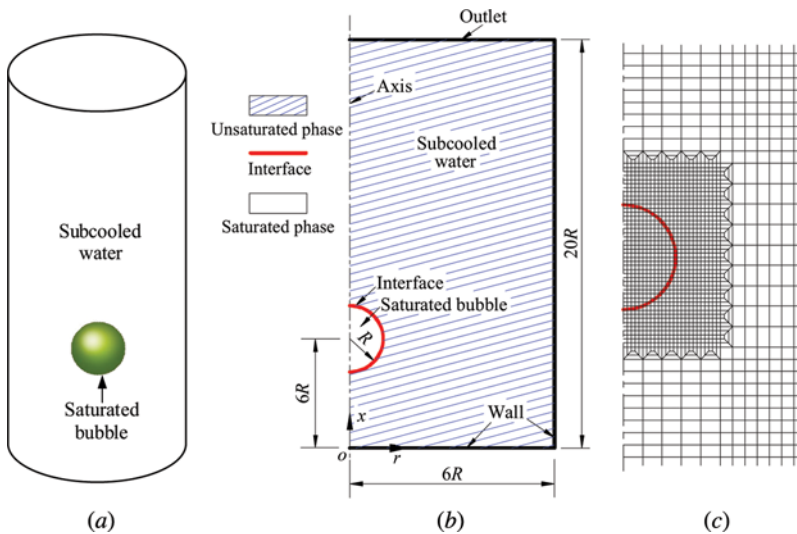


**Figure 11.** (a) Structure schematic diagram, (b) computation region, and (c) grid system for single-bubble condensation problem.
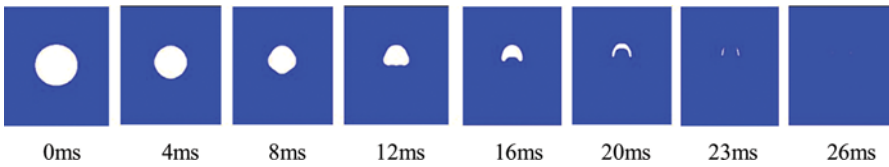
**Figure 12.** Bubble deformation during condensation with 15 mm in the initial bubble diameter.

$6R$ and $20R$, where $R$ denotes the bubble initial radius. The ratio of the distance between the bubble center and pool wall to the bubble initial radius is kept to be larger than 6 to eliminate the effects of the pool wall. No-slip velocity boundary conditions are applied on the bottom and side walls, and the wall heat fluxes are set as zero. The axis line is set as the axial boundary condition. The top outlet is considered ast the pressure outlet boundary condition. The velocity is initialized to be zero. The initial subcooling degree is 20 K, i.e., $\Delta T = T_{\text{sat}} - T_{\text{water}} = 20$ K. The corresponding grid system is illustrated in Figure 11$c$. The grid size increases along the bubble center direction. The different grid sizes are linked with each other by adopting a transition pattern. The minimum grid size near the bubble is set as $0.05$ mm$(r) \times 0.05$ mm $(x)$. Further grid refinement yields no significant improvement of the computation results.

Figure 12 illustrates the bubble shape sequences with 15 mm in initial bubble diameter. The bubble deformation during the condensation process is much more complicated than that of an adiabatic bubble. It can be found that the bubble experiences spherical, dimpled ellipsoidal, and skirted shapes, and finally splits into small fragments. Figure 13 shows the bubble lifetime at different initial bubble diameters obtained from Kamei's experiment [27], the moving-particle semi-implict (MPS) method [28], and the new phase-change model. As shown in Figure 13, the comparison results show good agreement, verifying the accuracy of the new model.
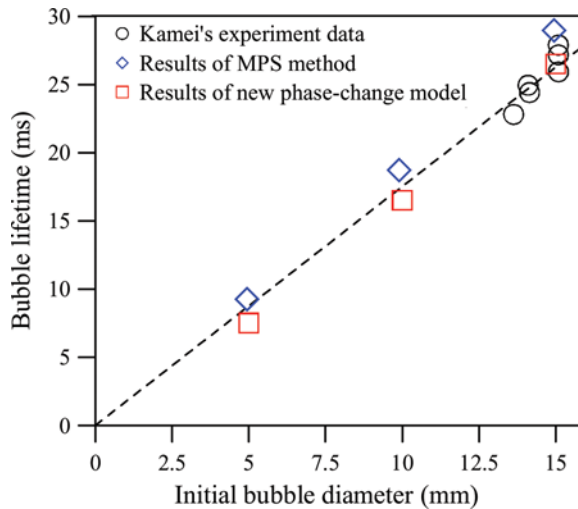


**Figure 13.** Comparison of bubble lifetime between Kamei's experiment and two different simulation methods.

## 4. CONCLUSION

In this article, a new phase-change model is developed using user-defined functions (UDFs), based on the volume-of-fluid (VOF) method in the FLUENT code. The model is suitable for the case in which one phase is unsaturated and the other is saturated. Its implementation process includes the following three parts.

1. Assume that the thermal conductivity of the saturated phase is equal to that of the unsaturated phase, i.e., $\lambda_s = \lambda_{uns}$.
2. The interfacial mass transfer fluxes ($\dot{m}_l$ and $\dot{m}_v$) at $C_I$ are derived by the heat exported from $C_I$ and $C_{Is}$ for the condensation process, or the heat imported in $C_I$ and $C_{Is}$ for the evaporation process.
3. The heat source term ($S_h$) at $C_I$ is calculated by the heat exported from $C_I$ for the condensation process, or the heat imported in $C_I$ for the evaporation process. The temperature at $C_{Is}$ is set as the saturated temperature by the large coefficient method.

The new phase-change model can obtain grid-independent and accurate results, which has been verified by three two-phase flow and heat transfer problems. In the future, this model will be extended to the case in which both two phases can be in the unsaturated state.

## FUNDING

## REFERENCES

1. C. W. Hirt and B. D. Nichols, Volume of Fluid (VOF) Method for the Dynamics of Free Boundary, *J. Comput. Phys.*, vol. 39, pp. 201–225, 1981.
2. D. L. Youngs, Time-Dependent Multi-Material Flow with Large Fluid Distortion, in K. W. Morton and M. J. Baines (eds.), *Numerical Method for Fluid Dynamics*, pp. 273–285, Academic Press, New York, 1982.
3. M. Huang, L. L. Wu, and B. Chen, A Piecewise Linear Interface-Capturing Volume-of-Fluid Method Based on Unstructured Grids, *Numer. Heat Transfer B*, vol. 61, pp. 412–437, 2012.
4. S. Osher and J. A. Sethian, Fronts Propagating with Curvature Dependent Speed: Algorithms Based on Hamilton-Jacobi Formulations, *J. Comput. Phys.*, vol. 79, pp. 12–49, 1988.
5. S. Osher and R. P. Fedkiw, Level Set Methods: An Overview and Some Recent Results, *J. Comput. Phys.*, vol. 169, pp. 463–502, 2001.
6. P. T. Wang, H. W. Sun, P. Y. Wong, H. Fukuda, and T. Ando, Modeling of Droplet-Based Processing for the Production of High-Performance Particulate Materials Using the Level Set Method, *Numer. Heat Transfer A*, vol. 61, pp. 401–416, 2012.

7. S. W. J. Welch and J. Wilson, A Volume of Fluid Based Method for Fluid Flows with Phase Change, *J. Comput. Phys.*, vol. 160, pp. 662–682, 2000.

8. M. W. Akhtar and S. J. Kleis, Boiling Flow Simulations on Adaptive Octree Grids, *Int. J. Multiphase Flow*, vol. 53, pp. 88–99, 2013.

9. S. S. Jeon, S. J. Kim, and G. C. Park, Numerical Study of Condensing Bubble in Subcooled Boiling Flow Using Volume of Fluid Model, *Chem. Eng. Sci.*, vol. 66, pp. 5899–5909, 2011.

10. L. M. Pan, Z. W. Tan, D. Q. Chen, and L. C. Xue, Numerical Investigation of Vapor Bubble Condensation Characteristics of Subcooled Flow Boiling in Vertical Rectangular Channel, *Nuclear Eng. Des.*, vol. 248, pp. 126–136, 2012.

11. H. Ganapathy, A. Shooshtari, K. Choo, S. Dessiatoun, M. Alshehhi, and M. Ohadi, Volume of Fluid-based Numerical Modeling of Condensation Heat Transfer and Fluid Flow Characteristics in Microchannels, *Int. J. Heat Mass Transfer*, vol. 65, pp. 62–72, 2013.

12. W. H. Lee, A Pressure Iteration Scheme for Two-Phase Flow Modeling, in T. N. Veziroglu (ed.), *Multiphase Transport Fundamentals, Reactor Safety, Applications*, Hemisphere, Washington, DC, 1980.

13. H. L. Wu, X. F. Peng, P. Ye, and Y. Eric Gong, Simulation of Refrigerant Flow Boiling in Serpentine Tubes, *Int. J. Heat Mass Transfer*, vol. 50, pp. 1186–1195, 2007.

14. S. C. K. De Schepper, G. J. Heynderichx, and G. B. Marin, Modeling the Evaporation of a Hydrocarbon Feedstock in the Convection Section of a Steam Cracker, *Comput. Chem. Eng.*, vol. 33, pp. 122–132, 2009.

15. A. Alizadehdakhel, M. Rahimi, and A. A. Alsairafi, CFD Modeling of Flow and Heat Transfer in a Thermosyphon, *Int. Commun. Heat Mass Transfer*, vol. 37, pp. 312–318, 2010.

16. Z. Yang, X. F. Peng, and P. Ye, Numerical and Experimental Investigation of Two Phase Flow during Boiling in a Coiled Tube, *Int. J. Heat Mass Transfer*, vol. 51, pp. 1003–1016, 2008.

17. C. Fang, M. David, A. Rogacs, and K. Goodson, Volume of Fluid Simulation of Boiling Two-Phase Flow in a Vapor-Venting Microchannel, *Frontiers Heat Mass Transfer*, vol. 1, pp. 1–11, 2010.

18. D. Z. Guo, D. L. Sun, Z. Y. Li, and W. Q. Tao, Phase Change Heat Transfer Simulation for Boiling Bubbles Arising from a Vapor Film by VOSET Method, *Numer. Heat Transfer A*, vol. 59, pp. 857–881, 2011.

19. A. Nichita and J. R. Thome, A Level Set Method and a Heat Transfer Model Implemented into Fluent for Modeling of Microscale Two Phase Flows, AVT-178 Specialists' Meeting on System Level Thermal Management for Enhanced Platform Efficiency, 2010.

20. W. B. Mao, Numerical Simulation of Vapor-Liquid Phase Change Heat Transfer and Micromixing in Microfluidic Systems, Master's thesis, GuangZhou Institute of Energy Conversion Chinese Academy of Sciences, China, 2009.

21. D. L. Sun, J. L. Xu, and L. Wang, Development of a Vapor-Liquid Phase Change Model for Volume-of-Fluid Method in FLUENT, *Int. Commun. Heat Mass Transfer*, vol. 39, pp. 1101–1106, 2012.

22. J. U. Brackbill, D. B. Kothe, and C. Zemach, A Continuum Method for Modeling Surface Tension, *J. Comput. Phys.*, vol. 100, pp. 335–354, 1992.

23. W. Q. Tao, *Numerical Heat Transfer*, 2nd ed., Xi'an Jiaotong University Press, Xi'an, China, 2001, pp. 244–245.

24. G. Son and V. K. Dhir, Numerical Simulation of Film Boiling Near Critical Pressures with a Level Set Method, *J. Heat Transfer*, vol. 120, pp. 183–192, 1998.

25. V. Alexiades and A. D. Solomon, *Mathematical Modeling of Melting and Freezing Processes*, Hemisphere, Washington, DC, 1993.

26. V. V. Klimenko, Film Boiling on a Horizontal Plate—New Correlation, *Int. J. Heat Mass Transfer*, vol. 24, pp. 69–79, 1981.
27. S. Kamei and M. Hirata, Condensation Phenomena of Single Vapor Bubble into Sub-cooled Water (1st Report Flow Visualization), *JSME Ser. B*, vol. 53, pp. 464–469, 1987.
28. W. X. Tian, Y. Ishiwatari, S. Ikejiri, M. Yamakawa, and Y. Oka, Numerical Computation of Thermally Controlled Steam Bubble Condensation using Moving Particle Semi-Implicit (MPS) Method, *Ann. Nuclear Energy*, vol. 37, pp. 5–15, 2010.